Synthesis of the Nanoscale Phosphor $(Y_{0.95}Tb_{0.05})_2O_2CO_3$ by Alkalide Reduction and Its Phase Transformation to $(Y_{0.95}Tb_{0.05})_2O_3$

Olivera Zivkovic, Kim E. Mooney, and Michael J. Wagner*

Department of Chemistry, The George Washington University, 725 21st Street NW, Washington, D.C. 20052

Received February 24, 2007. Revised Manuscript Received May 5, 2007

$(Y_{0.95}Tb_{0.05})_2O_2CO_3$ nanoparticles have been synthesized by subambient homogeneous reduction using alkalide solutions and subsequent oxidation. As synthesized, the material consists of free flowing agglomerates of ill-defined, amorphous, or subnanocrystalline nanoparticles. Thermal analysis shows that 2.83 CO_2 molecules are adsorbed per Y_2O_3 formula unit in the washed product. The samples annealed at 200 °C or greater are crystalline, consisting of agglomerated nanocrystals. The nanocrystals grow from an average of 15.3−17.6 nm, the agglomerates decrease in size, and the surface area decreases from 88 to 78 m^2/g as the annealing temperature is raised from 400 to 700 °C. Annealing at 800 °C results in a phase change from the carbonate to $(Y_{0.95}Tb_{0.05})_2O_2$. The crystallite size of the oxide phase increases from 21.4 to 22.6 nm, and the surface area increases from 82 to 86 m^2/g as the annealing temperature is increased from 800 to 1000 °C. Transmission electron microscopy observations show that the increase in the surface area, even as the average crystallite size increases, is consistent with the breaking up of agglomerates and the creation of a highly textured material, probably due to the release of CO_2 during the phase transition. The washed unannealed product displays luminescence typical of the Tb^{3+} ion. The photoluminescence intensity of the green $^5D_4-^7F_4$ transition increases with increasing annealing temperature, from 5% for the unannealed product to 16% for the nanophosphor annealed at 1000 °C.

Introduction

Phosphors that are capable of low voltage excitation are required for the development of low power, portable field emission displays (FEDs).[1] Traditional bulk phosphors are typically inefficient at low excitation potential due to shallow electron penetration depth, resulting in the excitation of only a small fraction of the phosphor. This limitation may be overcome by the use of nanoscale phosphors, whose physical dimensions can be on the order of the electron penetration depth, thus enabling excitation of all of the phosphor at low potentials. In addition, nanoscale phosphors could enable smoother films with higher fill, enhanced resolution, and luminescence enhancement due to quantum confinement.[2−8]

Y_2O_3:Tb is an efficient green phosphor, which as an oxide, it is expected to be stable when interacting with the electron beam and not release gases that can poison the field emitting tips of an FED.[1,9] The synthesis of nanoscale Y_2O_3:Tb by sol−gel,[5] unspecified microemulsion techniques,[10,11] and combustion[12] has been reported by other investigators. Here we report the synthesis of nanocrystalline $(Y_{0.95}Tb_{0.05})_2O_2CO_3$ by alkalide reduction and its transformation to nanocrystalline $(Y_{0.95}Tb_{0.05})_2O_3$.

Alkalides are crystalline ionic salts consisting of crown ether or cryptand complexed alkali metal cations charge balanced by a stoichiometric number of alkali metal anions.[13,14] Alkalides produce alkali metal anions when dissolved in non-reducible solvents. The alkali metal anion is nearly as thermodynamically powerful a reductant as a solvated electron, the most powerful reductant possible in any given solvent, and is capable of simultaneous two electron transfers. Alkalide reduction of metal salts results in the formation of a colloid of nanoscale (∼2−15 nm diameter) particles. Colloid stability varies from minutes to hours, depending on the metal reduced and the reaction conditions. Following aggregation and removal of the solvent, the byproducts can be washed away, recovering the

* To whom correspondence should be addressed.

(1) Holloway, P. H.; Trottier, T. A.; Abrams, B.; Kondoleon, C.; Jones, S. L.; Sebastian, J. S.; Thomes, W. J.; Swart, H. *J. Vac. Sci. Technol., B* **1999**, *17*, 758.
(2) Tissue, B. M. *Chem. Mater.* **1998**, *10*, 2837.
(3) Holmes, J. D.; Ziegler, K. J.; Doty, R. C.; Pell, L. E.; Johnston, K. P.; Korgel, B. A. *J. Am. Chem. Soc.* **2001**, *123*, 3743.
(4) Bhargava, R. N.; Gallagher, D.; Hong, X.; Nurmikko, A. *Phys. Rev. Lett.* **1994**, *72*, 416.
(5) Goldburt, E. T.; Kulkarni, B.; Bhargava, R. N.; Taylor, J.; Libera, M. *J. Lumin.* **1997**, *72*−*74*, 190.
(6) Wakefield, G.; Keron, H. A.; Dobson, P. J.; Hutchison, J. L. *J. Colloid Interface Sci.* **1999**, *215*, 179.
(7) Sharma, P. K.; Jilavi, M. H.; Nass, R.; Schmidt, H. *J. Lumin.* **1999**, *82*, 187.
(8) Jungnickel, V.; Henneberger, F. *J. Lumin.* **1996**, *70*, 238.
(9) Itoh, S.; Toki, H.; Sate, Y.; Morimoto, K.; Kishino, T. *J. Electrochem. Soc.* **1991**, *138*, 1509.
(10) Bhargava, R. N.; Chhabra, V.; Kulkarni, B.; Veliadis, J. V. *Phys. Status Solidi B* **1998**, *210*, 621.
(11) Soo, Y. L.; Huang, S. W.; Kao, Y. H.; Chhabra, V.; Kulkarni, B.; Veliadis, J. V.; Bhargava, R. N. *Appl. Phys. Lett.* **1999**, *75*, 2464.
(12) Wang, J.; Song, H.; Sun, B.; Ren, X.; Chen, B.; Xu, W. *Chem. Phys. Lett.* **2003**, *379*, 507.
(13) Wagner, M. J.; Dye, J. L. *Annu. Rev. Mater. Sci.* **1993**, *23*, 223.
(14) Wagner, M. J.; Dye, J. L. Alkalides and Electrides. In *Comprehensive Supramolecular Chemistry*; Lehn, J. M., Gokel, G. W., Eds.; Elsevier: Oxford, U.K., 1996; Vol. 1, p 477.

10.1021/cm0705183 CCC: $37.00
Published on Web 06/13/2007

crown ether and leaving bare metal nanoparticles. Supported as well as bare particles can be produced.[15−18]

Previous studies showed the general applicability of the alkalide reduction method to producing nanoparticles of elements from p-block semi-metals to the early transition metals and even the rare earths.[15−17,19−21] The synthesis of carbides,[22,23] nitrides,[24] binary oxides[25] of the early transition metals, ternary ferrites,[26] and oxide nanorods[27] as well as alloys and intermetallics[15,16,20] have been reported. In addition, the synthesis of nanocrystalline red phosphor $(Y_{0.95}Eu_{0.05})_2O_3$ by post-alkalide reduction oxidation of $Y_{0.95}Eu_{0.05}$ alloy nanoparticles during the removal of byproducts was reported.[28] Here we extend that study with the synthesis of nanocrystalline green phosphor $(Y_{0.95}Tb_{0.05})_2O_2CO_3$ by a similar post-alkalide reduction treatment of nanoparticulate $(Y_{0.95}Tb_{0.05})$ alloy and its transformation to $(Y_{0.95}Tb_{0.05})_2O_3$.

Experimental Section

Nanoscale yttrium−terbium metal alloy was synthesized by homogeneous alkalide reduction according to the following scheme:

$$3K^+(\text{15-crown-5})_2Na^- + 1.9YCl_3 + 0.1TbCl_3 \xrightarrow[-40\ °C]{\text{THF}} 2(Y_{0.95}Tb_{0.05})_{\text{nano}} + 3K^+(\text{15-crown-5})_2Cl^- + 3NaCl$$

Direct exposure of the product to air results in oxidation that generates sufficient heat to decompose the crown ether byproduct, making it very difficult to remove by washing. Thus, oxidation of the alloy was performed in two stages. First, a thin layer of the raw product was formed by spreading it onto an aluminum foil in an inert atmosphere glovebox prior to exposing it to air. Once removed from the glovebox, the material was immediately immersed in aerated H_2O at ambient temperature which was used to further oxidize the product and remove the byproducts. The product was separated from the wash by centrifuge ($15{,}500 \times g$). Washing was repeated 10 times to ensure complete removal of the byproducts.

YCl_3 and $TbCl_3$ (both anhydrous, 99.99%, packed under Argon) were purchased from Aldrich, and crown ether (15-crown-5, 98%) was purchased from Alfa Aesar. Tetrahydrofuran (THF, 99.9+% HPLC grade, inhibitor free) was purified by stirring over KNa alloy until a persistent blue solution was obtained. Reaction vessel loading was performed in a N_2 filled drybox (<1 ppm H_2O and O_2), and solvent transfers were accomplished by vacuum techniques (10^{-6} Torr). Samples (0.15 g) were annealed in a tube furnace after flame sealing under vacuum (10^{-6} Torr) in fused silica tubes (volume = 4.5 mL).

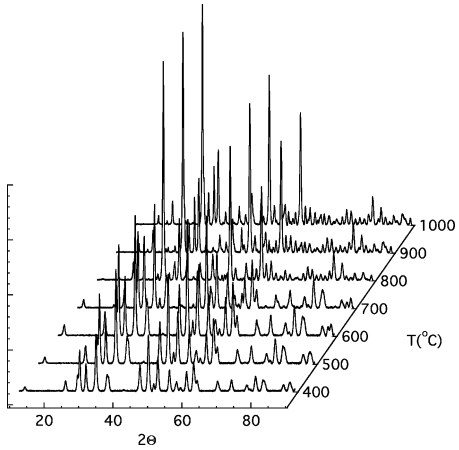

Figure 1. Powder XRD patterns of the nanocrystalline materials reported in this study annealed for 4 h at the indicated temperatures.

Electron micrographs were obtained on a JEM-1200EX transmission electron microscope operating at 80 keV. Samples for transmission electron microscopy (TEM) were dispersed in MeOH by sonication and deposited on Formvar holey film/carbon coated copper grids. Powder X-ray patterns were obtained with a Rigaku Miniflex diffractometer (Cu Kα radiation). Thermal analysis, differential calorimetric analysis (DTA), and thermogravimetric analysis (TGA) were performed on Perkin-Elmer DTA-7 and Pyris TGA-1 instruments, respectively, under flowing N_2 gas (20 mL/min). Infrared spectra were obtained with a Perkin-Elmer Spectrum RX FT-IR spectrometer. Elemental analysis was obtained by X-ray fluorescence (Kratos Analytical EDX-700).

Surface area measurements were made on a custom (in-house) built adsorption apparatus using the BET method with N_2 as the absorption gas and the sample immersed in a liquid N_2 bath. The system is based on classical designs and uses two burettes with 11 Hg filled bulbs to vary total volume. Pressure was measured with a MKS Instruments 870B capacitance manometer using a 660-B10 power supply/display. The vapor pressure of N_2 at the adsorption temperature (P_0) was measured directly with a Hg manometer. Samples were degassed for 4 h at 400 °C under vacuum (10^{-6} Torr) prior to adsorption measurements. Photoluminescence measurements were performed on a Shimadzu RF-5301PC spectrofluorimeter at ambient temperature. Quantum yields were determined by comparison with the photoluminescence of sodium salicylate excited at the same wavelength as the corresponding sample.[29,30]

Results and Discussion

The material obtained after washing with aerated H_2O is a free flowing white powder. Elemental analysis found the Tb doping level to be 5%, unchanged from the reaction stoichiometry. Fourier transform infrared spectra show that while the material is free of organic byproducts, it does contain a significant quantity of adsorbed CO_2. Powder X-ray diffraction (XRD) showed only broad features indicating that the particles are either amorphous or subnanocrystalline.

Annealing the material for 4 h at temperatures as high as 300 °C resulted in no significant change in powder XRD; material that was annealed for 4 h at 400 °C displayed a crystalline pattern consistent with $(Y_{0.95}Tb_{0.05})_2O_2CO_3$ with no other detectable phases (Figure 1). The occurrence of a carbonate phase is in contrast to the results of our previous

(15) Tsai, K.-L.; Dye, J. L. *J. Am. Chem. Soc.* **1991**, *113*, 1650.
(16) Dye, J. L.; Tsai, K. L. *Faraday Discuss.* **1991**, *92*, 45.
(17) Tsai, K. L.; Dye, J. L. *Chem. Mater.* **1993**, *5*, 540.
(18) Cowen, J. A.; Tsai, K. L.; Dye, J. L. *J. Appl. Phys.* **1994**, *76*, 6567.
(19) Nelson, J. A.; Bennett, L. H.; Wagner, M. J. *J. Am. Chem. Soc.* **2002**, *124*, 2979.
(20) Nelson, J. A. Synthesis and Characterization of Nanomaterials by Alkalide Reduction. Ph.D., The George Washington University, Washington, DC, 2002.
(21) Nelson, J. A.; Bennett, L. H.; Wagner, M. J. *J. Mater. Chem.* **2003**, *13*, 857−60.
(22) Nelson, J. A.; Wagner, M. J. *Chem. Mater.* **2002**, *14*, 1639.
(23) Nelson, J. A.; Wagner, M. J. *Chem. Mater.* **2002**, *14*, 4460.
(24) Chen, X. Z.; Dye, J. L.; Eick, H. A.; Elder, S. H.; Tsai, K.-L. *Chem. Mater.* **1997**, *9*, 1172.
(25) Nelson, J. A.; Wagner, M. J. *Chem. Mater.* **2002**, *14*, 915.
(26) Mooney, K. E.; Nelson, J. A.; Wagner, M. J. *Chem. Mater.* **2004**, *16*, 3155.
(27) Nelson, J. A.; Wagner, M. J. *J. Am. Chem. Soc.* **2003**, *125*, 332.
(28) Nelson, J. A.; Brant, E. L.; Wagner, M. J. *Chem. Mater.* **2003**, *15*, 688.
(29) Tregellas-Williams, J. *J. Electrochem. Soc.* **1958**, *105*, 173.
(30) Allison, R.; Burns, J.; Tuzzolino, A. J. *J. Opt. Soc.* **1964**, *54*, 747.

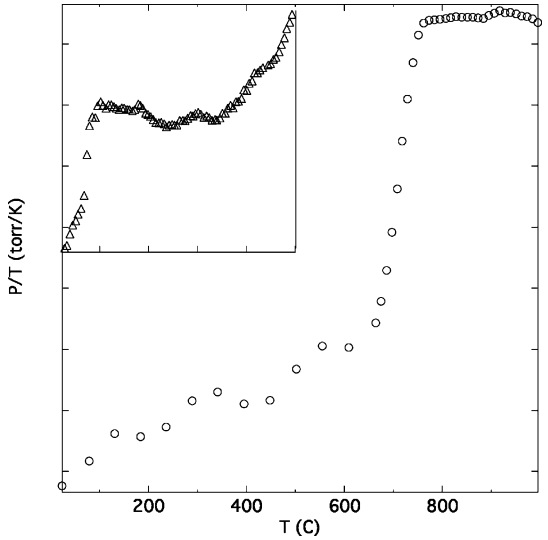

Figure 2. Plot of the reduced pressure as a function of annealing temperature on first annealing of the washed product (inset) and of the $(Y_{0.95}Tb_{0.05})_2O_2CO_3$ nanocrystals. Note, at the low pressures at which this experiment was conducted the reduced pressure is approximately proportional to the number of CO_2 molecules present.

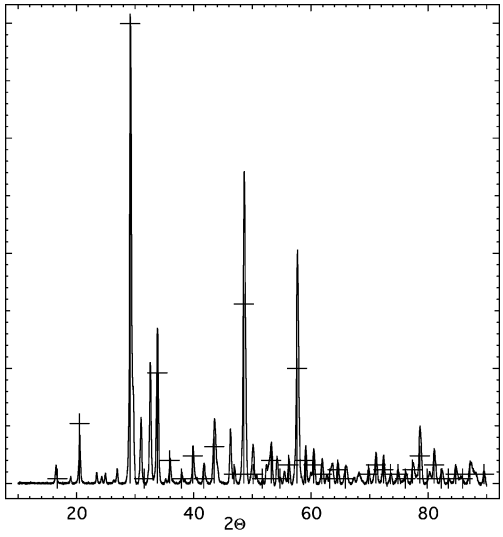

Figure 3. Powder XRD pattern of $(Y_{0.95}Tb_{0.05})_2O_3$ nanocrystals following annealing at 1000 °C for 4 h (solid line) and the standard pattern (JCPDS PDF no. 25-1011, peaks with crosses).

study of Y_2O_3:Eu for which only the oxide phase was observed. Whereas in the previous study the material had been annealed in air, in this study it was annealed in evacuated, sealed ampoules. Annealing in sealed, evacuated tubes was necessary to prevent the oxidation of Tb^{+3} to Tb^{+4}, changing the color of the material from white to orange and resulting in a product that displays no fluorescence. Annealing under active vacuum, rather than sealed tubes, resulted in a dark product that also does not fluoresce, presumably as a result of loss of oxygen from the Y_2O_3 structure.

Although the samples were sealed under vacuum prior to heating, opening the reaction tubes after heating revealed that the pressure had risen to more than 1 atm. In fact, annealing samples that were significantly larger than reported here (see Experimental Section) resulted in bursting of the reaction tube upon heating, indicating that the sample was the source of the pressure buildup. Examination of the gas present in the reaction tube with a residual gas analyzer (RGA), during and following heating, revealed that the high pressure was due to CO_2 gas apparently adsorbed to the washed nanomaterial and released upon heating. Under typical reaction conditions employed to obtain crystalline products at 400 °C, CO_2 pressure in the reaction tube was approximately 4.2 atm; this gas is in excess of that required for crystallization of the carbonate phase. TGA analysis of the synthetic product on first heating showed that 37% of the sample mass is lost as CO_2 upon heating. This corresponds to 2.83 CO_2 molecules for every $(Y_{0.95}Tb_{0.05})_2O_3$ formula unit in the unannealed material.

The pressure in the reaction tubes was measured upon first heating of small samples (Figure 2, inset). The reaction tubes were initially evacuated (10^{-6} Torr), and sample size was chosen such that the total pressure of the CO_2 evolved during heating would not exceed 50 Torr. Significant desorption is observed below 100 °C; RGA measurements show that this rise in pressure is due to the release of weakly bound (physisorbed) CO_2. More strongly (chemisorbed) CO_2 is released at temperatures in excess of ~350 °C. Note that the annealing conditions used for this desorption experiment resulted in the formation of the pure oxide rather than the carbonate phase; much higher CO_2 pressure is required for carbonate formation.

Annealing the $(Y_{0.95}Tb_{0.05})_2O_2CO_3$ at 700 °C results in the appearance of cubic $(Y_{0.95}Tb_{0.05})_2O_3$ as a minor phase detectable by XRD. Further annealing at higher temperature results in further transformation of the carbonate into the oxide phase. The transformation to the oxide phase is virtually complete after annealing at 800 °C; however, a minor unidentified impurity phase appears at and persists even after annealing at 1000 °C (Figure 3).

The transformation of the carbonate to the oxide was followed by observing the evolution of CO_2 and the resultant rise in pressure during the annealing of nanocrystalline $(Y_{0.95}Tb_{0.05})_2O_2CO_3$ in an initially evacuated (10^{-6} Torr), sealed fused silica tube. The quantity of carbonate was chosen so that the total pressure remained less than 100 Torr throughout the temperature range studied. Moderate CO_2 desorption is observed above 100 °C, increasing modestly with increasing temperature to 600 °C (Figure 2). As no phase change is detected in the XRD patterns in this temperature range, the observed desorption is most likely due to the release of adsorbed CO_2. A sharp increase in CO_2 desorption is observed with an onset of ~650 °C, co-incident with the phase transformation of the carbonate to the oxide. These data are in good agreement with DTA measurements which show a broad irreversible endothermic peak in the thermogram upon heating with an onset of 644 °C and $\Delta H = 180.7$ J/g. Note, the desorption and DTA measurements were conducted in a vacuum and at atmospheric pressure, respectively. Annealing of the nanophosphor used for other measurements reported in this manuscript was done initially in evacuated, sealed fused silica ampoules; evolution of CO_2 during annealing increased the pressure to many atmospheres, suppressing the transition from carbonate to oxide by Le Chatelier's Principle. Thus, the phase transition from the carbonate to the oxide phase observed in the powder XRD shown in this manuscript occurs at a somewhat higher

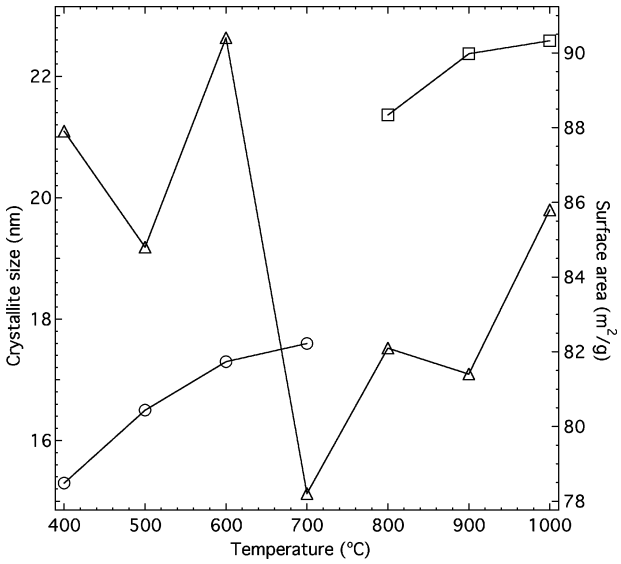

Figure 4. Average crystalline size determined form X-ray line broadening of the $(Y_{0.95}Tb_{0.05})_2O_2CO_3$ (circles) and $(Y_{0.95}Tb_{0.05})_2O_3$ (squares) and the surface area (triangles) as functions of annealing temperature. The lines connecting data points are to guide the eye. Samples were annealed for 4 h at the given temperature.

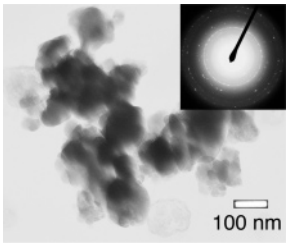

Figure 5. TEM micrograph of $(Y_{0.95}Tb_{0.05})_2O_2CO_3$ nanocrystal agglomerates after annealing at 200 °C for 4 h. Inset is a selected area diffraction (SAD) pattern consistent with $(Y_{0.95}Tb_{0.05})_2O_2CO_3$.

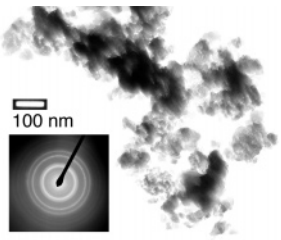

Figure 6. TEM micrograph of $(Y_{0.95}Tb_{0.05})_2O_2CO_3$ nanocrystal agglomerates after annealing at 300 °C for 4 h. Inset is a SAD pattern consistent with $(Y_{0.95}Tb_{0.05})_2O_2CO_3$.

temperature than that observed in desorption and DTA measurements, whereas the transition was observed to be ~1/3 complete at 700 °C by desorption measurements and complete by 775 °C; the material used for the other measurements showed the oxide phase to be a minor component after annealing at 700 °C and the carbonate phase to persist as a minor component after annealing at 800 °C. It should be noted that the minor unidentified impurity phase noted above is not observed after annealing during the desorption and DTA measurements; apparently the impurity phase is only generated when the annealing is conducted under significant CO_2 pressure.

The powder XRD peaks sharpen with increasing annealing temperature indicating crystallite growth (Figure 1). The crystallite size of the carbonate phase, as determined from XRD line broadening, increases from 15.3 to 17.6 nm as the annealing temperature is raised from 400 to 700 °C (Figure 4). The phase transformation from carbonate to oxide is very nearly complete after annealing at 800 °C; the oxide phase has an average crystallite size 21.4 nm after annealing at 800 °C that grows slightly to 22.6 nm after annealing at 1000 °C.

The surface area of the material, measure by the BET method, first decreases and then increases, with the net result of a slight increase from 88 to 90 m^2/g as the annealing temperature was raised from 400 to 600 °C (Figure 4). A sharp decrease in the surface area is observed after annealing at 700 °C even though little change is observed in the crystallite size. This decline coincides with the onset of the phase transition from carbonate to oxide; the loss of accessible surface area may be due to intercrystallite growth of the oxide phase blocking access to individual grains. Steady growth of the surface area, from 78.2 to 85.8 m^2/g, is observed as the annealing temperature is raised from 700 to 1000 °C and the phase transformation progresses.

The unannealed material was found to be composed of ill-defined agglormerates in which it is difficult to distinguish individual nanoparticles, similar to those seen for the previously reported Eu doped nanomaterial.[28] Annealing the material results in the breakup of these agglomerates to form more defined nanoparticles. Although no crystalline phase can be detected in the XRD patterns of products annealed below 400 °C, examination of the products by TEM reveals crystallinity after annealing at temperatures as low as 200 °C (Figure 5). This indicates that the crystallites are too small (<1−2 nm) to be observed in powder XRD patterns. The nanocrystallites are strongly agglomerated, and thus distinguishing individual crystallites in the TEM micrographs is also difficult.

Increasing the annealing temperature results in the reduction of the size of the agglomerates (Figure 6); individual nanocrystallite size correlates reasonably well with the XRD crystallite size for samples annealed at temperatures between 400 and 600 °C. The agglomerates become noticeably looser after annealing at 600 °C, separating the previously adjoined nanocrystallites and exposing additional surfaces; this decrease in interparticle interaction accounts for the observed increase in BET surface area. This phenomenon may be related to the phase transition from carbonate to oxide. The transition is observed by DTA to have an onset temperature of ~644 °C, corresponding well to a sharp increase in CO_2 release observed in desorption measurements, which might seem to rule out its significance for a surface area increase that occurs after annealing at or below 600 °C. However, significant CO_2 desorption is seen from 500 °C to 600 °C; the escape of this gas may be responsible for the looser agglomerate structure observed.

Annealing at 700 °C causes many of the individual nanocrystallites to conjoin indicating sintering (Figure 7); this is consistent with the observed sharp decrease in the BET surface area with only a small increase in crystallite size as determined from XRD line broadening. Annealing at higher temperatures results in an increase in the surface area as the agglormerates break up, even as the average

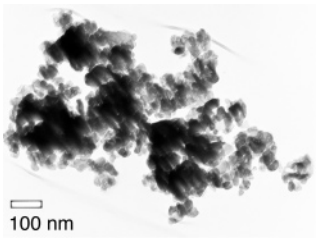

Figure 7. TEM micrograph of $(Y_{0.95}Tb_{0.05})_2O_2CO_3$ (major phase) and $(Y_{0.95}Tb_{0.05})_2O_3$ (minor phase) nanocrystal agglomerates after annealing at 700 °C for 4 h.

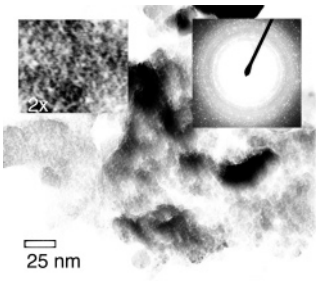

Figure 8. TEM micrograph of $(Y_{0.95}Tb_{0.05})_2O_3$ nanocrystal agglomerates after annealing at 700 °C for 4 h. Inset (upper right) is 2× magnification showing the highly textured nature of the material. Inset (upper left) is the SAD pattern consistent with $(Y_{0.95}Tb_{0.05})_2O_3$.

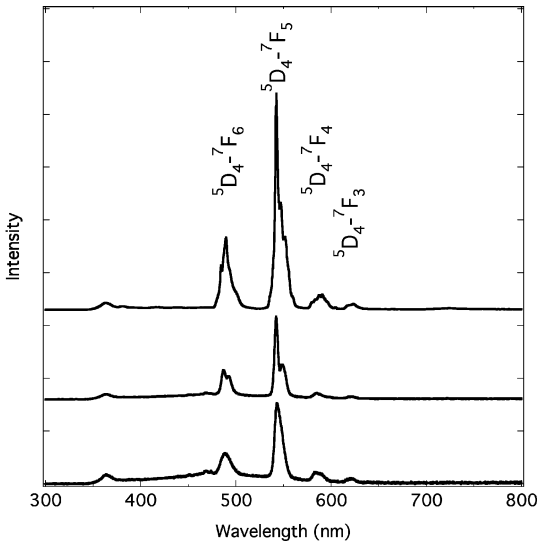

Figure 9. Photoluminescence spectra of unannealed nanoparticulate $(Y_{0.95}Tb_{0.05})_2O_2CO_3$ (bottom), nanocrystalline $(Y_{0.95}Tb_{0.05})_2O_2CO_3$ after annealing at 400 °C for 4 h (middle), and nanocrystalline $(Y_{0.95}Tb_{0.05})_2O_3$ after annealing at 1000 °C for 4 h (top).

crystallite size increases. The morphology of the material dramatically changes as the reaction proceeds; the release of gas from the nanocrystallites results in a highly textured surface, accounting for the observed increase in BET surface area even as the average crystallite size increases (Figure 8).

In contrast to the behavior observed for the previously reported europium doped Y_2O_3 nanoscale phosphor,[28] fluorescence can be observed from the unannealed terbium doped product. Photoluminescence spectra display emission typical of transitions $^5D_4-^7F_J$ of the Tb^{3+} ion (Figure 9). Featureless emission peaks are observed for unannealed material; peak structure consistent with sublevels due to crystal field splitting can be observed after annealing the material to 400 °C and higher, co-incident with crystallization observed in powder XRD spectra.

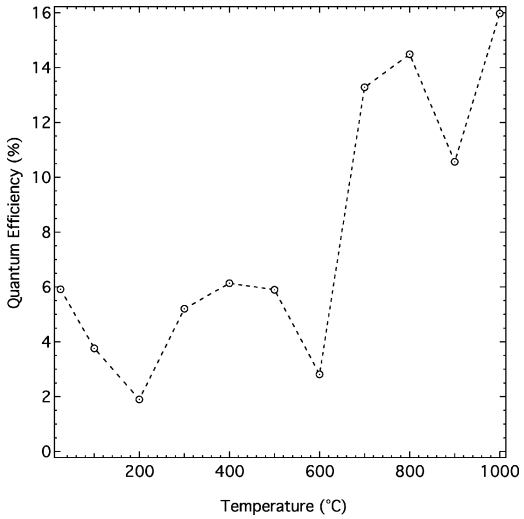

Figure 10. Quantum efficiency (%) for the $^5D_4-^7F_4$ transition of the nanophosphors excited at their wavelength of maximum efficiency (see Figure 11) plotted as a function of annealing temperatures. The lines connecting data points are to guide the eye.

The quantum efficiency of the phosphors generally increases with increasing nanocrystallite size, as might be expected because the increase in size implies a decrease in surface recombination sites, contrary to the findings of other investigators.[5] However, this correlation is not perfect as the behavior is significantly complicated by the evolution of gas during heating and the phase change from carbonate and oxide, resulting in morphology, texture, size, and crystalline structure changes. The quantum efficiency of the emission initially decreases with annealing to temperatures as high as 200 °C, increases and plateaus from 300−500 °C, decreases again following annealing at 600 °C, increases sharply after annealing to 700 and 800 °C, and decreasing and then finally increasing to 16% for the green $^5D_4-^7F_4$ transition following annealing at 900 and 1000 °C, respectively (Figure 10). The combined quantum efficiency of all of the transitions reaches a maximum of 35%; however, it is important to note that in applications as a green phosphor, only luminescence from the $^5D_4-^7F_4$ transition would be utilized.

The low temperature (up to 200 °C) decrease in fluorescence intensity coincides with the observation of significant CO_2 evolution and the breaking up of the ill-defined agglomerates of the unannealed material to form more defined but still aggregated nanoparticles, although surface area measurements were not conducted because of difficulties in obtaining complete degassing of the surface without heating the samples, and it is reasonable to conclude from the TEM observations that the loss of CO_2 resulted in an increase in the materials surface area. Thus, the decrease in the quantum efficiency upon annealing as high as 200 °C can reasonably be assumed to be due to an increase in surface recombination.

The decrease in quantum efficiency observed in samples annealed from 500 °C to 600 °C, despite a slight increase in crystallite size, is probably associated with the measured increase in surface area and, consequently, surface recombination observed in the same temperature range. The larger than fourfold increase in quantum efficiency that occurs following annealing at 700 °C coincides with the onset of

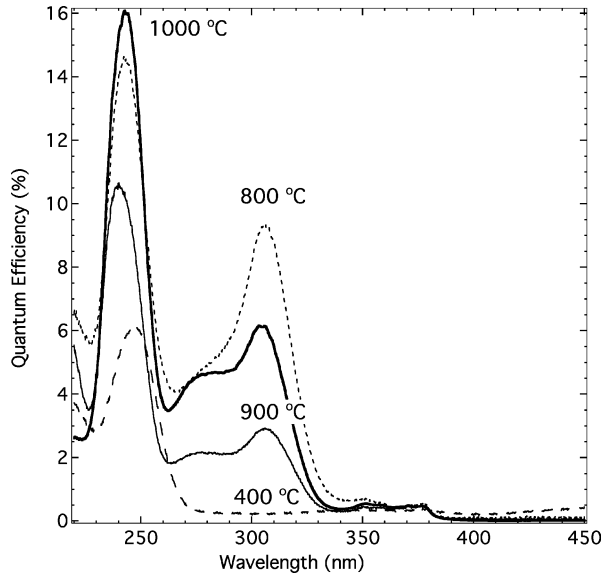

Figure 11. Photoluminescence quantum efficiency for the $^5D_4-^7F_4$ transition of nanocrystalline $(Y_{0.95}Tb_{0.05})_2O_2CO_3$ after annealing at 400 °C (heavy dashed line) and $(Y_{0.95}Tb_{0.05})_2O_3$ after annealing at 800 °C (dashed line), 900 °C (solid line), and 1000 °C (heavy solid line) plotted as a function of excitation wavelength.

the carbonate to oxide phase change, a sharp decrease in surface area with only a small increase in crystallite size, and apparent nanoparticle sintering observed in TEM images. The presence of the oxide is unlikely to explain the increase in quantum efficiency as it is a minor phase. More likely, a reduction in surface quenching sites due to the sharp decrease in surface area is responsible for the observed increase.

Typical photoluminescence excitation spectra ($^5D_4-^7F_5$ emission) for the carbonate and oxide phases are shown in Figure 11. The spectra for the $(Y_{0.95}Tb_{0.05})_2O_2CO_3$ samples annealed at various temperatures are essentially identical once corrected for differences in their quantum efficiencies, having a single broad peak at ~247 nm. The spectra are very similar to that of material described as nonaggregated Y_2O_3:Tb nanoparticles made by an unspecified microemulsion technique, with identical peak position but somewhat more narrow and lacking the shoulder reported at 305 nm.[10] To our knowledge, no reports of the excitation or fluorescence spectra of the terbium doped carbonate, either as bulk or nanocrystalline material, have appeared in any previous publication.

Following transformation to $(Y_{0.95}Tb_{0.05})_2O_3$, this peak shifts to 243 nm and a new feature is observed with a maximum at 306 nm, with a broad shoulder connecting the two peaks. These spectra are significantly different from that reported for 35 nm (determined from XRD line broadening) nanocrystalline material made by combustion,[12] which in turn appears to be identical to that reported for bulk material.[11] The 243 nm peak of the excitation spectra of the nanocrystalline material reported here is located at 20 nm lower wavelength and does not have the lower wavelength shoulder observed for the major peak of the bulk material. The peak at 306 nm is broader and red-shifted 5 nm from that of the presumably equivalent feature in the bulk spectra. The spectra are, however, in good agreement, both in position and breadth, with those reported for material described as aggregated Y_2O_3:Tb, although the intensity of the 243 nm peak is significantly larger relative to the 306 nm peak than was reported for material made by an unspecified microemulsion technique.[10]

Conclusions

The synthesis of nanoscale Y_2O_3:Tb phosphor by alkalide reduction is somewhat more complicated than that of the analogous Y_2O_3:Eu reported previously.[28] To prevent the oxidation of Tb^{+3} to Tb^{+4}, the product must be annealed in evacuated tubes, rather than in air as was done for the previous reported Y_2O_3:Eu. The release of adsorbed CO_2, presumably accumulated while washing the product in air, can result in a high gas pressure in the sealed tube and the formation of the carbonate, $(Y_{0.95}Tb_{0.05})_2O_2CO_3$, rather than the oxide. The carbonate is strongly fluorescent and may be applicable as a phosphor; however, it seems unlikely to be useful as a FED phosphor as it may outgas during electron beam excitation. The carbonate does transform into the oxide, which is even more strongly fluorescent, with a maximum quantum yield of 16% for the green $^5D_4-^7F_4$ transition after annealing at 1000 °C. Furthermore, the nanocrystalline oxide is highly textured with a high surface area, physical characteristics that are likely to be advantageous in application as FED phosphors.

Acknowledgment. We thank the National Science Foundation for financial support (DMR-0504925).

CM0705183